Structural Durability & Health Monitoring

Tech Science Press

https://doi.org/10.32604/sdhm.2026.081186

ARTICLE

Research on the Chloride Ion Penetration Resistance of Manufactured Sand Concrete Based on WOA-Adam Hybrid Optimized BPNN

Zhichao Liu[1,2], Jun Zhang[2,*], Dongling Yu[3], Libing Jin[1] and Bingquan Song[3]

[1]School of Civil Engineering, Henan University of Technology, Zhengzhou, China
[2]School of Civil Engineering and Architecture, Ningbo Technology University, Ningbo, China
[3]Ningbo Communications Engineering Construction Group Co., Ltd., Ningbo, China

*Corresponding Author: Jun Zhang. Email: zj@nbt.edu.cn

Received: 25 February 2026; Accepted: 15 April 2026; Published: 24 August 2026

ABSTRACT: The chloride ion penetration resistance of manufactured sand concrete (MSC) critically determines the durability of marine concrete structures. However, its accurate prediction is challenging due to high uncertainty from complex influencing factors. To address this, a back-propagation neural network model optimized by a hybrid Whale Optimization Algorithm and Adaptive Moment Estimation strategy (WOA-Adam-BPNN) was developed to predict the electrical flux. The model was trained and tested on 245 experimental datasets covering eight key parameters and validated across four typical mix proportions. Results show that the WOA-Adam hybrid strategy effectively combines global search capability with adaptive convergence, significantly enhancing model performance. The proposed model achieved a mean absolute percentage error (MAPE) of 4.01%, a root mean square error (RMSE) of 59.57, and a coefficient of determination (R^2) of 0.9879, significantly outperforming both the traditional Adam-BPNN and the genetic algorithm-optimized Adam-BPNN (GA-Adam-BPNN) models and the WOA-XGB hybrid model (WOA-XGB). Moreover, it maintains a stable prediction error within 5% across common engineering parameter ranges. This study provides a reliable reference for the mix proportion design and durability assessment of MSC.

KEYWORDS: Manufactured sand; chloride ion penetration resistance; electric flux; machine learning; WOA-Adam-BPNN

1 Introduction

With the increasingly tight supply of natural sand resources, manufactured sand (MS) and gravel aggregates have become the main source of construction materials. According to statistics, the total global demand for sand and gravel aggregates for use in construction is estimated to be between 56 and 58 billion tonnes in 2024. Take China for example, the proportion of MS stone in the 15.2 billion tons of sand and gravel has exceeded 80% [1–4]. The large-scale application of MS significantly supports the sustainable development of the construction industry. However, the durability of MSC structures during long-term service has not garnered sufficient attention [5,6]. The chloride erosion resistance of concrete is primarily governed by its pore structure and density. First, the characteristics of the parent rocks of MS—including its gradation, particle morphology, and stone powder content—differ substantially from those of natural sand [7,8]. Second, the distinct morphology and gradation of MS particles frequently impair concrete workability, necessitating the addition of mineral admixtures (e.g., fly ash or slag) to alleviate this issue [9]. Furthermore, the diverse sources of MS result in significant variations in its mineral composition and stone powder content. These variations further complicate the prediction of chloride ion penetration resistance in MSC. Consequently, the chloride ion penetration resistance of MSC has exhibited significant uncertainty. Moreover, conventional concrete mix proportion design methods struggle to precisely account for the specific material properties of MSC and complex service environments. These methods rely heavily on time-consuming and resource-intensive physical tests, which often yield limited sample data and, consequently, models with poor generalizability [10].

Against this backdrop, machine learning (ML) offers a novel approach for addressing the complex nonlinear problems associated with these materials. For instance, Hong et al. [11] combined artificial neural networks (ANN) with Hong-Lagrange method, reducing the cost and weight of concrete beams by 30.1% and 10.4%, respectively. Similarly, Hao et al. [12] integrated ML with genetic algorithms to develop an intelligent design method for fly ash concrete, demonstrating the advantages of XGBoost and gradient boosting (GB) models in predicting strength and slump. Al-Taai et al. [13] employed Bayesian optimization (BO) to tune an XGBoost model for predicting the compressive strength of eco-friendly concrete incorporating granulated blast furnace slag and recycled coarse aggr This does not correspond to the list of references. Please check.egates. In a study on concrete strength prediction, Lyngdoh et al. [14] reported that XGBoost achieved the highest predictive accuracy when the dataset was interpolated using a k-nearest neighbor (kNN) algorithm configured with 10 neighbors configured. Tian et al. [15] demonstrated that a WOA-optimized BPNN yielded the highest prediction accuracy for both the chloride ion flux and compressive strength of polymer-modified waterproof mortar. Jiang et al. [16] proposed a predictive model integrating Bayesian optimization with stacked ensemble learning, which provided relatively accurate estimates for the compressive strength of MSC. Collectively, these studies underscore the significant potential of ML methods in predicting material properties. It should be noted that while backpropagation neural networks (BPNN) can effectively capture intrinsic correlations within complex systems, they suffer from drawbacks such as lengthy training times, a tendency to converge to local optima, and vanishing gradient problems [17,18]. The WOA algorithm achieves broad exploration of the solution space through random encirclement during the initial phase, followed by fine exploitation via contraction encirclement and spiral updates in subsequent phases. This strategy helps mitigate issues like particle aggregation (common in particle swarm optimization) and premature convergence (prevalent in genetic algorithms). However, WOA algorithm exhibits a relatively slow convergence speed when applied to the weight optimization of neural networks [15]. In contrast, the Adam algorithm efficiently achieves local convergence by combining estimates of the first and second moments of gradients with an adaptive learning rate [19,20]. Therefore, integrating the complementary advantages of WOA (global exploration), Adam (efficient local tuning), and BPNN (nonlinear fitting) into a hybrid neural network architecture provides a promising solution to the aforementioned limitations.

To overcome the vanishing gradient and overfitting problems inherent in the high-dimensional parameter optimization of traditional BPNNs, this study proposes a hybrid strategy. This strategy leverages the fine convergence capability of the Adam stage and the global search ability of the WOA stage to escape local optima. Consequently, the model's prediction accuracy and generalization ability under multi-factor coupling conditions are significantly enhanced. Finally, experimental verification was conducted through four types of mix proportion tests, with the key variables being the manufactured sand replacement rate, fly ash content, stone powder content, and water-cement ratio. This design aimed to rigorously validate the model's predictive performance across a range of practical conditions. Although existing studies have combined intelligent optimization algorithms with machine learning for concrete performance prediction, research on hybrid optimization models for chloride ion penetration characteristics of MSC remains scarce. Most relevant models only involve simple improvements of a single optimization algorithm, lacking customized optimization logic designed for the engineering small-sample, multi-parameter strong nonlinearity features of this research field.

2 WOA-Adam-BPNN Model

2.1 Model Introduction

2.1.1 Back Propagation Neural Network (BPNN)

The Back-Propagation Neural Network (BPNN) is a typical feedforward neural network composed of an input layer, hidden layers, and an output layer, with excellent nonlinear mapping capabilities. The network calculates the output through forward propagation, and continuously updates weights and biases via error back-propagation using gradient descent to minimize the prediction error. After multiple iterative trainings, BPNN can gradually make the output approach the true value, thereby accomplishing regression fitting and prediction tasks.

(1) Forward Propagation (Output Calculation)

$$z = Wx + b \tag{1}$$

$$y = f(z) \tag{2}$$

where: x = input; W = weight; b = bias; $f(\cdot)$ = activation function; y = network output.

(2) Loss function (taking mean squared error as an example)

$$E = \frac{1}{2}\sum_{i=1}^{n}(y_i - \hat{y}_i)^2 \tag{3}$$

where: E = loss function; y_i = true value; $\hat{y}_i$ = predicted output of the network.

(3) Backpropagation (Weight Update)

$$\Delta w = -\eta\frac{\partial E}{\partial w} \tag{4}$$

$$w_{new} = w_{old} + \Delta w \tag{5}$$

where: η = learning rate.

2.1.2 eXtreme Gradient Boosting (XGBoost)

XGBoost is an ensemble learning algorithm based on gradient boosting. It uses additive models to accumulate the prediction results of multiple decision trees.

(1) Additive model

$$\hat{y}_i = \sum_{k=1}^{K} f_k(x_i) \tag{6}$$

where: $\hat{y}_i$ = Predicted value of sample i; k = Total number of decision trees; f_k = Function of the Kth decision tree.

(2) The objective function in the t-th round (second-order Taylor expansion)

$$\mathcal{L}^{(t)} \approx \sum_{i=1}^{n}\left[g_i f_t(x_i) + \frac{1}{2}h_i f_t(x_i)^2\right] + \Omega(f_t) \tag{7}$$

where: g_i and h_i represent the first and second derivatives of the loss function respectively. By using Taylor expansion, the loss function is approximated as a quadratic function with respect to the new tree f_t, which facilitates optimization.

(3) Regular term

$$\Omega\left(f_t\right) = \gamma T + \frac{1}{2}\lambda \sum_{j=1}^{T} w_j^2 \tag{8}$$

where: γ = Leaf count penalty coefficient; T = Total number of leaf nodes of the t-th tree; λ = L2 regularization coefficient; w_j = Weight (output score) of the j-th leaf node.

(4) Optimal leaf weight

$$w_j^* = -\frac{G_j}{H_j + \lambda}, \quad G_j = \sum_{i \in I_j} g_i,\ H_j = \sum_{i \in I_j} h_i \tag{9}$$

where: G_j = The sum of the first-order derivatives of all samples falling on leaf j; H_j = The sum of the second-order derivatives of all samples falling on leaf j; I_j = The sample set that is classified to leaf j.

(5) Structural score (tree quality)

$$\mathcal{L}_{\text{struct}} = -\frac{1}{2}\sum_{j=1}^{T}\frac{G_j^2}{H_j + \lambda} + \gamma T \tag{10}$$

where: All symbols are the same as above.

(6) Splitting gain

$$\text{Gain} = \frac{1}{2}\left[\frac{G_L^2}{H_L + \lambda} + \frac{G_R^2}{H_R + \lambda} - \frac{\left(G_L + G_R\right)^2}{H_L + H_R + \lambda}\right] - \gamma \tag{11}$$

G_L, H_L: The sum of the first and second derivatives of all samples on the left child node after the split;

G_R, H_R: The sum of the first and second derivatives of all samples on the right child node after the split.

2.2 Introduction to Optimization Algorithms

2.2.1 Adaptive Moment Estimation Algorithm (Adam)

Adam is a gradient-based optimization algorithm based on adaptive moment estimation. By combining the advantages of the momentum method method and RMSprop, it achieves dynamic adjustment of the learning rate. The algorithm utilizes the first-order and second-order moment estimates of the gradient to assign independent learning rates to different parameters, and ensures stability in the initial stage of iteration through bias correction. With fast convergence speed and strong robustness, Adam is a commonly used and efficient optimizer for training neural networks. Its core formulas are as follows:

$$m_t = \beta_1 \cdot m_{t-1} + \left(1 - \beta_1\right) \cdot g_t \tag{12}$$

$$v_t = \beta_2 \cdot v_{t-1} + \left(1 - \beta_2\right) \cdot g_t^2 \tag{13}$$

$$\theta_t = \theta_{t-1} - \alpha \cdot \frac{\hat{m}_t}{\sqrt{\hat{v}_t} + \varepsilon} \tag{14}$$

where: g_t = gradient, α = learning rate, β_1, β_2 = exponential decay rates, ϵ = small constant to prevent division by zero.

2.2.2 Whale Optimization Algorithm (WOA)

Whale Optimization Algorithm (WOA) is an intelligent optimization algorithm inspired by the hunting behavior of humpback whales, achieving optimization through prey encircling, spiral position update and random search. By means of a convergence factor and probability selection, the algorithm balances global exploration and local exploitation, featuring few parameters, simple structure and fast convergence speed. With high optimization accuracy and strong robustness, it is suitable for parameter optimization and objective optimization of complex nonlinear models.

(1) Encircling and Shrinking

$$D = |C \cdot X^{*}(t) - X_i(t)| \tag{15}$$

$$X(t+1) = X^{*}(t) - A \cdot D \tag{16}$$

$$A = 2\mathrm{a} \cdot \mathrm{r} - \mathrm{a} \tag{17}$$

$$C = 2\mathrm{r} \tag{18}$$

where: t = iteration number; X^{*} = position vector of the current optimal solution; X = position vector of the individual; D = distance between the individual and the prey; A and C = coefficient vectors for the movement mode of whales.

(2) Spiral Updating

$$X(t+1) = D\mathrm{q} \cdot e^{bl} \cdot \cos(2\pi l) + X^{*}(t) \tag{19}$$

where: Dq = distance between a whale and the current best position; b = a constant for defining the shape of the spiral; l = a random number uniformly distributed in the range [−1, 1].

(3) Random Search

$$D^{*} = |C \cdot X\mathrm{rand}(t) - X(t)| \tag{20}$$

$$X(t+1) = X\mathrm{rand}(t) - A \cdot D^{*} \tag{21}$$

where: $X\mathrm{rand}(t)$ = random position vector of a whale individual; D = distance between the random whale individual and the current searching individual; $X(t+1)$ = updated position of the current whale individual.

2.2.3 Genetic Algorithm (GA)

Genetic Algorithm (GA) is an intelligent optimization algorithm that simulates the process of biological evolution. It iteratively evolves the population through selection, crossover, and mutation. The algorithm evaluates individuals by the fitness function, retains individuals with high fitness, and generates better offspring. It has the characteristics of strong global search ability and good robustness, and is widely used in model parameter optimization and objective optimization problems.

(1) Fitness Function

$$f_i = \frac{1}{E_i} \tag{22}$$

(2) Selection Probability (Roulette Wheel Selection)

$$Pi = \frac{f_i}{\sum \frac{N}{j=1} f_j} \tag{23}$$

(3) Crossover Operation

$$X_1^{'} = \alpha X_1 + (1 - \alpha) X_2 \tag{24}$$

$$X_2^{'} = (1 - \alpha) X_1 + \alpha X_2 \tag{25}$$

(4) Mutation Operation

$$X' = X + (r_2 - r_1) \cdot \delta \tag{26}$$

where: f_i = individual fitness; E_i = model error; *Pi*: selection probability of the individual; X_1, X_2 = parent individuals; α = crossover coefficient; δ = mutation disturbance term; N: = population size.

2.3 Construct the WOA-Adam-BPNN Model

Architecture Overview: As illustrated in Fig. 1, the WOA-Adam-BPNN model is composed of two core computational modules: A deep neural network and a hybrid optimization strategy.

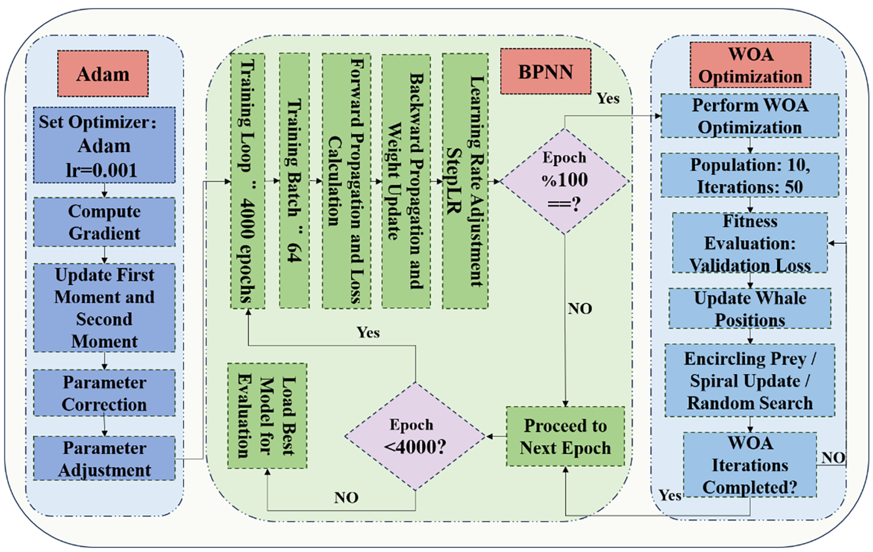

Figure 1: Training workflow of the WOA-Adam-BPNN hybrid optimization model.

Deep Neural Network Design: The deep neural network module employs a multi-layer feedforward architecture. Its depth and width are designed in accordance with feature representation learning principles, enabling feature abstraction and compression via progressive dimensionality reduction. Additionally, a Dropout layer is introduced to mitigate the risk of overfitting. The activation functions were selected based on an analysis of gradient propagation. The ReLU function in the hidden layers facilitates gradient flow via sparse activation, while a linear function in the output layer ensures continuous mapping for the regression task. This configuration facilitates complete modeling from feature extraction to final prediction.

Hybrid Optimization Strategy: The hybrid optimization module integrates Adam and WOA into a complementary two-stage strategy, and this strategy forms the core training process depicted in Fig. 1. In the initial training phase, Adam facilitates rapid parameter update and convergence via adaptive moment estimation. The optimizer then switches to WOA for the subsequent phase. WOA performs global exploration across the loss landscape by simulating the foraging behaviors of humpback whales (e.g., encircling prey and bubble-net feeding) to escape local optima. Furthermore, the module incorporates a StepLR learning rate scheduler and the MSE loss function. The synergy between the sensitivity of MSE to outliers and the dynamic adjustment of learning rate stabilizes the training process and guides the model toward a more generalizable solution, thereby enhancing predictive accuracy. This strategy—first converging to a high-quality local optimal domain, then global fine search—effectively mitigates traditional BPNN's premature convergence and the imbalance between convergence speed and global search capability of single optimizers.

3 Prediction of the Resistance of MSC to Chloride Ion Erosion

3.1 Data Collection and Preprocessing

Authoritative literature on the chloride ion penetration resistance of MS were systematically reviewed and analyzed, and finally 245 sets of valid sample data of MSC were selected. The detailed data sources are given in Table 1.

Table 1: Data sources [21–67].

Author	Collection Quantity	Author	Collection Quantity	Author	Collection Quantity
Wang et al. [21]	6	Sun et al. [37]	5	Xu et al. [53]	3
Liu et al. [22]	6	Zheng et al. [38]	5	Li et al. [54]	4
Li et al. [23]	7	Wu et al. [39]	3	Yan et al. [55]	5
Liu [24]	4	Wang et al. [40]	6	Yang et al. [56]	6
Zhang et al. [25]	5	Yang et al. [41]	5	Zhou et al. [57]	5
Li et al. [26]	4	Yan et al. [42]	10	Feng et al. [58]	6
Ge et al. [27]	9	Yu et al. [43]	8	Chandrasekhar and Ransinchung [59]	5
Walters and Jones [28]	2	Zhao et al. [44]	5	Liu et al. [60]	5
Narale and Jadhav [29]	3	Huang et al. [45]	5	Shanmugapriya et al. [61]	6
Li et al. [30]	5	Luo et al. [46]	4	Shanmugavadivu and Malathy [62]	3
Li et al. [31]	5	Wang et al. [47]	5	Zhang et al. [63]	5
Chang et al. [32]	6	Yu et al. [48]	5	Xu et al. [64]	2
Zhu et al. [33]	8	Tong et al. [49]	9	Balasubramaniam and Thirugnanam [65]	6
Shen et al. [34]	8	Guo et al. [50]	6	Qu et al. [66]	2
Dinh et al. [35]	5	Zhang et al. [51]	3	Jiang et al. [67]	5
Raja et al. [36]	5	Wang and Gao [52]	5		

Before model training, strict data filtering was conducted. Samples with missing test conditions, incomplete key parameters, or abnormal experimental results were excluded to ensure high data quality and reasonable distribution. The constructed database encompasses key parameters, including the manufactured sand replacement rate (MSR), coarse aggregate (CA), cement content (C), fly ash content (FA), stone powder content (SPC), water content (W), water-cement ratio (W/C), admixture dosage (A) and electric flux (EF), as detailed in Table 2.

Table 2: Statistical summary of the dataset.

Parameter	Unit	Min	Max	Mean	Std. Dev.
MSR	%	0	100	85.95	31.27
CA	kg/m^3	863	1242.48	1057.98	69.89
C	kg/m^3	188	517.75	358.57	75.9
FA	kg/m^3	0	225	71.89	50.18
SPC	%	0	30	8.29	6.41
W	kg/m^3	128	197.16	160.7	11.69
W/C	m_w/m_c	0.27	0.6	0.38	0.08
A	kg/m^3	0	17	5.15	3.37
EF	C	250	4500	1421.634	714.78

Fig. 2, Correlation matrix of the key parameters. As shown, EF has a positive correlation with W/C ($r = 0.39$). This indicates that an increase in W/C significantly increases EF, which directly leads to a decrease in the chloride ion penetration resistance of concrete. EF shows a moderate negative correlation with FA ($r = -0.33$). This suggests that the incorporating of an appropriate amount of FA can optimize the concrete microstructure via pore-filling and pozzolanic effects, thereby enhancing impermeability. Among the remaining parameters, EF exhibits relatively weak correlations with CA, SPC, MSR, and A ($|r| < 0.10$). Nonetheless, these parameters are retained as input variables because they represent key mix proportion components that are directly controllable in engineering practice and are thus essential for comprehensive durability assessment. Notably, SPC, despite its weak statistical correlation, serves as a critical indicator of MS quality, capturing its influence on concrete pore structure and impermeability. Based on this analysis, eight factors—namely MSR, CA, C, FA, SPC, W, W/C, and A—were selected as input variables, with EF serving as the output variable.

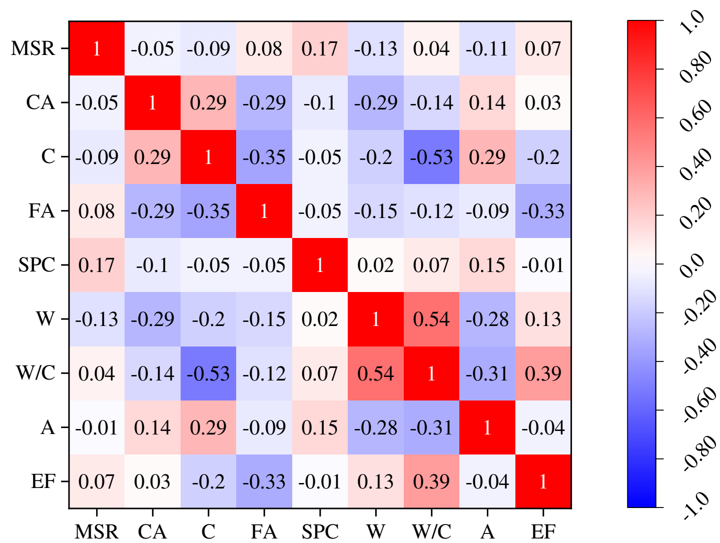

Figure 2: Correlation matrix.

To address the problem of missing values in the dataset and prevent their adverse effects on the stability of model training and the accuracy of prediction, a mean imputation method was employed for data repair. Specifically, the fillna function of the pandas library was used. This function computes the arithmetic mean of available (non-missing) values column-wise and uses this mean to impute missing entries in the respective columns. Furthermore, given the significant disparity in value ranges among the characteristic parameters in the original dataset (e.g., MSR varies from 0% to 100%), direct model input could lead to biased parameter weight estimation due to scale differences. It should be noted that mean imputation was conducted prior to normalization. Consequently, the complete dataset (with imputed values) was subjected to the MinMaxScaler transformation together with all other features. It should be noted that although the input parameters are interdependent, the missing rate is low, and mean imputation is a conservative approach that preserves the overall data distribution without introducing additional complexity from more advanced imputation methods.

In addition, other quality characteristics of MS, including particle shape, gradation, parent rock type, and methylene blue value, also significantly affect the chloride ion penetration resistance of MSC. However, due to the limited number of existing studies that systematically report these quality indicators, it is difficult to construct a sufficiently large and complete dataset. Accordingly, this study primarily adopts MSR and SPC as input variables, where SPC partially reflects key quality attributes of MS.

3.2 Model Training

To evaluate the generalization performance of the model, the dataset was divided into training and test sets at an 8:2 ratio. For the network architecture, a deep feedforward neural network with four hidden layers was employed. The number of neurons in the respective hidden layers is 64, 256, 512 and 128, with a one-dimensional output layer for the target variable. The Rectified Linear Unit (ReLU) function was chosen for the hidden layers due to its non-saturating gradient in the positive region, which helps mitigate the vanishing gradient problem and accelerates convergence. A linear activation function was used for the output layer to suit the numerical nature of the regression task. The specific hyperparameter configurations are summarized in Table 3.

Table 3: Hyperparameter settings.

Hyperparameter	Parameter Adjustment Range			
Hidden layer	1	2	3	4
Number of nodes	64	128	512	128
Batch size	64			
Learning rate	For every 4000 epochs, multiply the learning rate by 0.1			
Activation function	ReLU			

All hyperparameter configurations in Table 2 were determined via three rounds of comparative pre-experiments to the convergence speed, prediction accuracy and generalization ability of the model. The key optimization rationale is as follows: (1) The number of hidden layers was screened from 1 to 4, and 4 layers were selected for the optimal trade-off between fitting effect and overfitting risk; (2) The neuron combination of each hidden layer was optimized from 32 to 512 to achieve the best feature extraction ability for MSC multi-parameter data. To ensure complete reproducibility of all experimental results, a fixed random seed (7) was set for all Python libraries (NumPy, Scikit-learn, PyTorch) involved in data division, model initialization and optimization algorithm operation, eliminating randomness caused by different initial states.

In the first stage, the model underwent 4000 rounds of iterative learning. This approach takes advantage of the rapid initial convergence of the Adam optimizer while ensuring optimization quality. An initial learning rate of 0.001 was set, and Adam optimizer dynamically adjusted the step size for each parameter using its first-order and second-order moment estimates to achieve efficient and adaptive updates. This stage adhered to a strict three-step iterative process—forward propagation, backpropagation, and parameter update—to precisely control optimization and promote solution generalization. It was supplemented by two core strategies: First, key metrics—including the learning rate, training loss, and test loss—were logged every 100 rounds to monitor convergence dynamics and overfitting risk in real time. Second, an optimal model saving strategy was employed: parameters were saved only when the test set loss reached a new minimum, thereby ensuring the final model's generalization capability. Collectively, these measures ensured efficient and stable convergence of the model to a superior neighborhood of a local optimum. This laid a solid foundation for the subsequent global fine-tuning via the WOA. The second stage, optimization using the WOA, was crucial for enhancing model performance. The optimal model from the Adam-based training was loaded to serve as the initial population center for WOA. For WOA, a population size of 10 individuals was used, and 50 rounds of iterative optimization were conducted. During each iteration, WOA simulated three whale hunting behaviors: (1) encircling prey, selected with a 50% probability, with the search range controlled by a linearly decreasing convergence factor A; (2) performing a spiral update to simulate bubble-net attacks within the parameter space; and (3) conducting random searches in remaining cases to enhance the algorithm's ability to escape local optima. The fitness function was defined by the MSE loss on the test set. This ensured the optimization direction was aligned with improving the model's generalization ability.

Throughout the WOA phase, the optimization trajectory is rigorously monitored. The best fitness value is recorded per iteration, and the global optimum is updated in real-time when an improved solution is found. The final model is comprehensively evaluated on the independent test set using four key metrics: MAPE, MAE, RMSE, and R^2. This multi-dimensional assessment quantitatively validates the model's predictive performance. In summary, the proposed hybrid training framework, through the synergistic integration of Adam and WOA, successfully balances computational efficiency with the pursuit of optimal predictive accuracy.

3.3 Model Evaluation

Four evaluation metrics were employed: MAPE, MAE, RMSE, and R^2. Their calculation formulas are provided below. Lower values of MAPE, MAE, and RMSE indicate better model performance. R^2 measures the goodness of fit between predicted and actual values, ranging from 0 to 1. A value closer to 1 denotes a better fit and higher predictive accuracy.

$$MAPE = \frac{100\%}{m} \sum_{i=1}^{M} \left| \frac{\hat{y}_i - y_i}{y_i} \right| \tag{27}$$

$$MAE = \sum_{j=1}^{M} \left| \left(y_j' - y_j \right) \right| / M \tag{28}$$

$$RMSE = \sqrt{\sum_{j=1}^{M} \left(y_j' - y_j \right)^2 / M} \tag{29}$$

$$R^2 = 1 - \sum_{j=1}^{M} \left(y_j' - y_j \right)^2 / \sum_{j=1}^{M} \left(y_j - \overline{y} \right)^2 \tag{30}$$

In the formulas, M represents the number of samples in the dataset, y_j' is the true value of the sample, y_j is the predicted value of the sample, and $\overline{y}$ is the mean of the predicted values.

Fig. 3 compares the EF predictions of the four models against the actual measured values. Adam-BPNN, as a first-order optimizer, enhances training efficiency via momentum and adaptive learning rates. Nevertheless, it often converges to local optima in complex, non-convex loss landscapes. GA-Adam-BPNN employs a genetic algorithm for global weight optimization, which significantly reduces prediction errors. However, this approach is still prone to premature convergence. WOA-XGB integrates whale optimization with extreme gradient boosting, leveraging the feature learning advantages of tree models and the global search capability of WOA to achieve superior prediction accuracy, with its curve alignment clearly outperforming the two neural network models. In contrast, WOA-Adam-BPNN synergistically integrates the global exploration of WOA with the rapid local convergence of Adam. This integration enables the model to most accurately capture the system's nonlinear dynamics, resulting in a predicted curve that closely aligns with the measured data. In summary, the models' predictive performance ranks as follows: WOA-Adam-BPNN > WOA-XGB > GA-Adam-BPNN > Adam-BPNN.

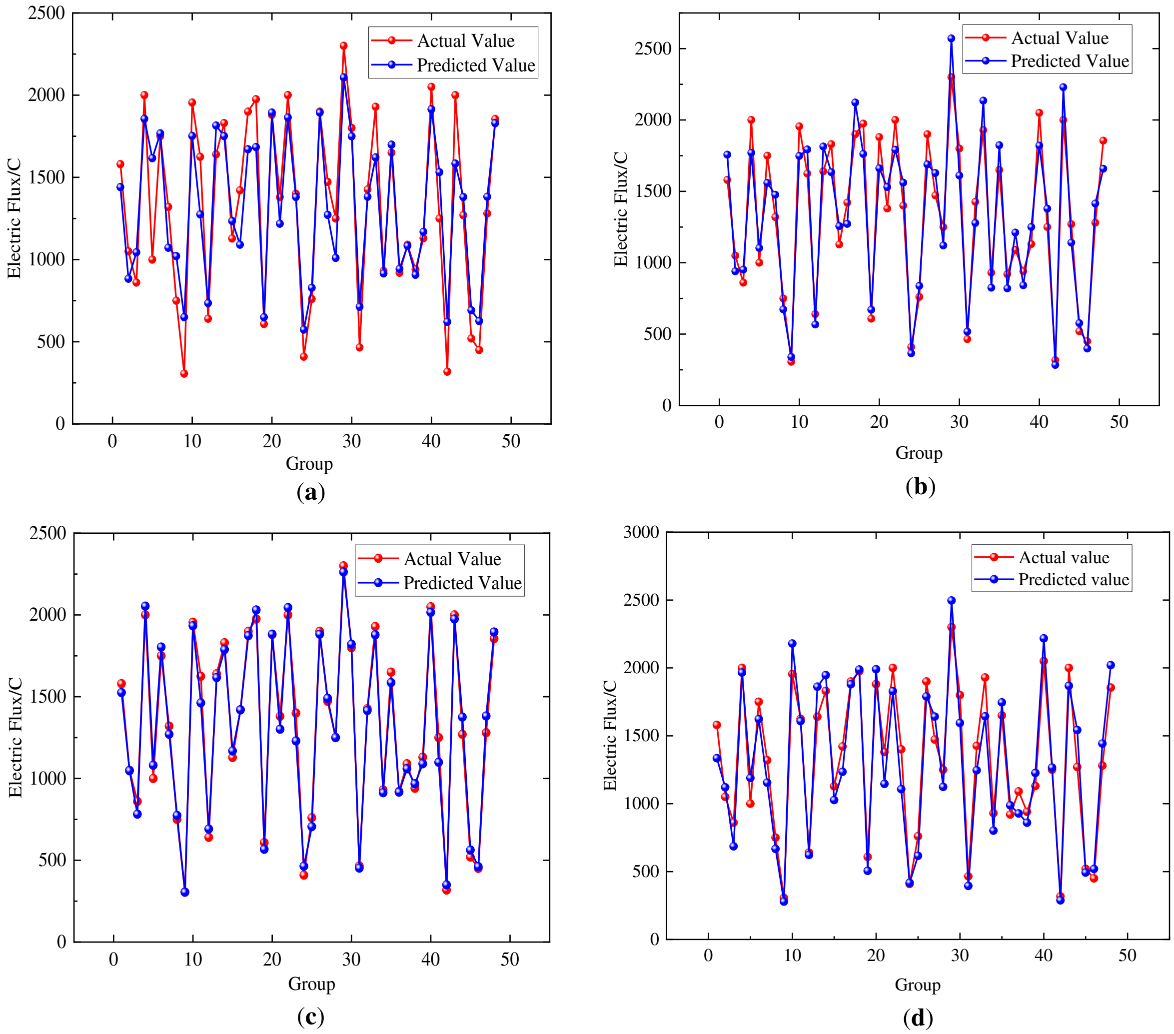

Figure 3: Comparison of predicted vs. actual EF values. (**a**) Adam-BPNN; (**b**) GA-Adam-BPNN; (**c**) WOA-Adam-BPNN; (**d**) WOA-XGB.

The error distributions depicted in Figs. 4 and 5 reveal a consistent and systematic hierarchy in the predictive performance of the four models. Analyzing absolute error (MAE), the Adam-BPNN model exhibits the widest fluctuation range (−416.44 to 616.47). The GA-Adam-BPNN model shows improvement, with a reduced range of −259.03 to 419.81, and the WOA-XGB model performs better with an absolute error range of −310.789 to 245.679. In contrast, the WOA-Adam-BPNN model demonstrates exceptional stability, confining errors to a significantly narrower interval of −170.36 to 105.11. This hierarchy is further corroborated by the relative error (MAPE). The Adam-BPNN model exhibits the broadest MAPE dispersion (0.32% to 0.95%). A marked improvement is observed for GA-Adam-BPNN (0% to 0.56%). The WOA-XGB model effectively lowers the relative error to 0%–50.3%, and most notably, the WOA-Adam-BPNN model maintains consistently superior accuracy, with its MAPE confined with in an exceptional range of 0% to 0.13%. Crucially, in both figures, the error trajectory of the WOA-Adam-BPNN model resides entirely within the error envelopes of the other three models. This provides a visual and conclusive demonstration of its superior stability and precision. Taken together, the evidence from both MAE and MAPE metrics conclusively establishes the following performance ranking: WOA-Adam-BPNN > WOA-XGB > GA-Adam-BPNN > Adam-BPNN.

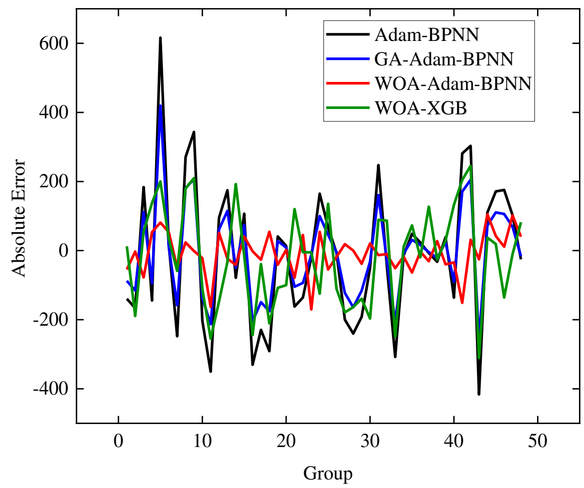

Figure 4: Absolute error of the three prediction models.

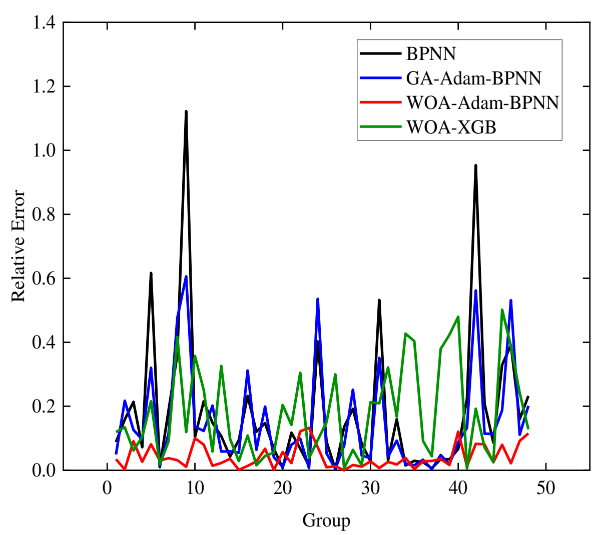

Figure 5: Relative error of the three prediction models.

Fig. 6 illustrates the predictive robustness of the four models (Adam-BPNN, GA-Adam-BPNN, WOA-XGB, and WOA-Adam-BPNN), evaluated on 196 training and 49 independent test samples. A clear performance gradient is evident between the training and test sets for all four models. The Adam-BPNN model achieves a training set R^2 of 0.8012. Notably, its performance on the test set is slightly better, with an R^2 of 0.8555. The GA-Adam-BPNN model demonstrates strong generalization capability, maintaining high fitting levels on both sets (training R^2 = 0.8824; test R^2 = 0.9028). This represents a 5.5% improvement in test set R^2 over the Adam-BPNN model, highlighting the efficacy of the genetic algorithm optimization. A further improvement is observed with the WOA-XGB model, which achieves a training R^2 of 0.9021 and a test R^2 of 0.9303, significantly outperforming the two neural network models. The WOA-Adam-BPNN model delivers the most outstanding performance. It not only attains a training R^2 of 0.9213 but also achieves a near-perfect fit on the test set, with an R^2 of 0.9879. Compared to WOA-XGB, this represents a 5.8% improvement in test set R^2, and compared to GA-Adam-BPNN, it represents a 9.4% improve; moreover, the WOA-Adam-BPNN model exhibits the smallest performance gap between the training and test sets. This minimal discrepancy indicates exceptional generalization ability and strong resistance to overfitting. In summary, the overall performance of the four models ranks as follows: WOA-Adam-BPNN > WOA-XGB > GA-Adam-BPNN > Adam-BPNN.

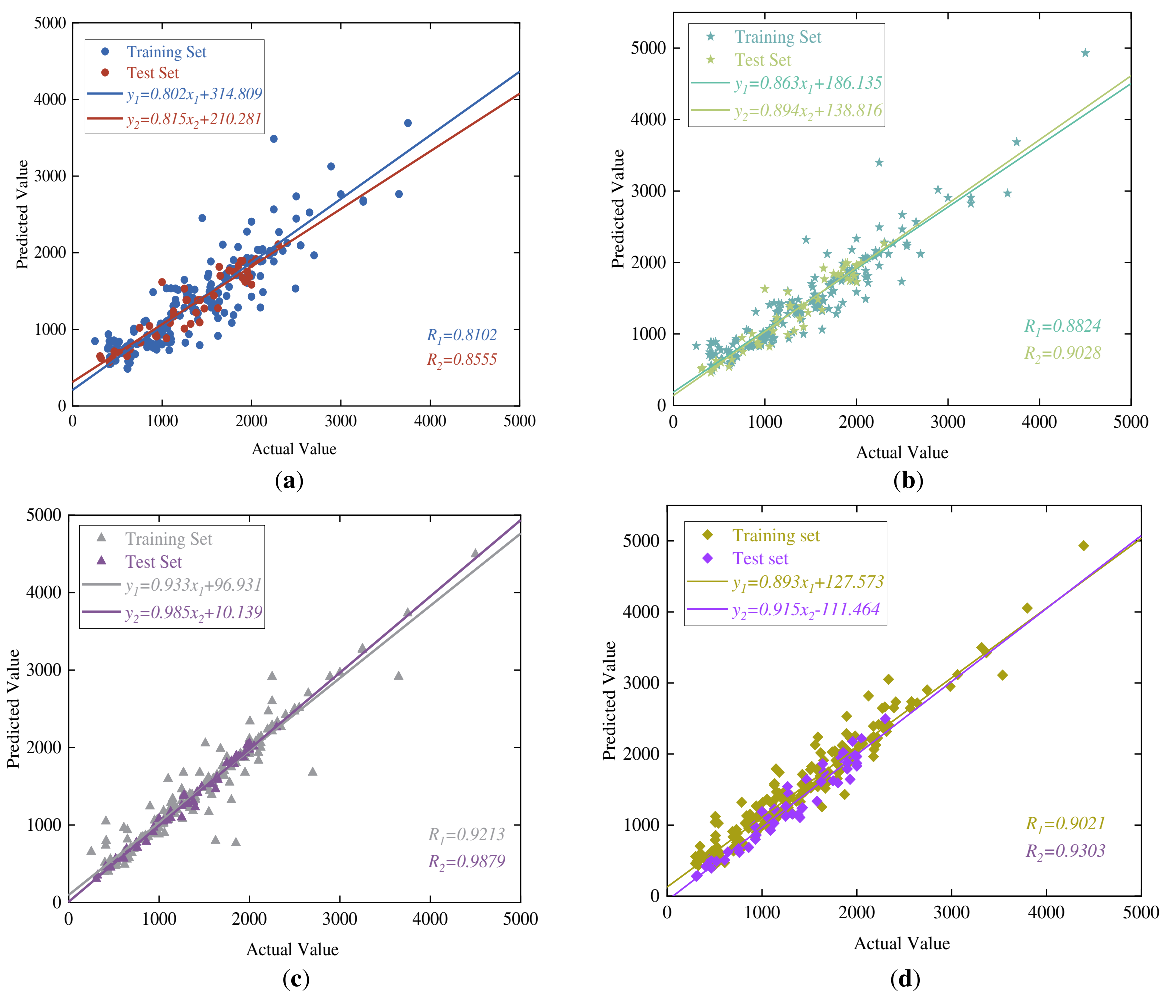

Figure 6: Distribution of training and testing sets. (**a**) Adam-BPNN; (**b**) GA-Adam-BPNN; (**c**) WOA-Adam-BPNN; (**d**) WOA-XGB.

Table 4 quantitatively summarizes the performance metrics of each model, highlighting the gradient differences in predictive capability among the four. Regarding the key error metrics, the Adam-BPNN model yields a MAPE of 17.65%, an MAE of 161.86, and an RMSE of 205.59. After optimization, the GA-Adam-BPNN model reduces these three metrics by 41.8%, 44.1%, and 41.4%, respectively. Building on this, the WOA-XGB model achieves further improvements, reducing MAPE, MAE, and RMSE by 52.2%, 53.5%, and 55.9% compared to Adam-BPNN. The WOA-Adam-BPNN model demonstrates the most remarkable performance, achieving drastically lower error metrics: MAPE = 4.01%, MAE = 45.09, and RMSE = 59.57. This corresponds to reductions of 77.3%, 72.1%, and 71.0% against Adam-BPNN; 61.0%, 50.2%, and 50.5% against GA-Adam-BPNN; and 52.5%, 40.1%, and 34.1% against WOA-XGB.

Table 4: Performance evaluation metrics of the prediction models.

Model	MAPE	MAE	RMSE	R^2
Adam-BPNN	17.65%	161.86	205.59	0.8555
GA-Adam-BPNN	10.28%	90.51	120.4	0.9028
WOA-XGB	8.45%	75.26	90.41	0.9303
WOA-Adam-BPNN	4.01%	45.09	59.57	0.9879

In summary, the hybrid WOA-Adam optimization strategy confers substantial multifaceted improvements upon the BPNN model. This is achieved through a synergistic, two-phase mechanism: (1) The Adam optimizer ensures rapid initial convergence via adaptive learning and momentum, furnishing a high-quality starting point; (2) Subsequently, the WOA algorithm is activated, employing its global search strategy. By simulating whale foraging behaviors (e.g., bubble-net predation), WOA performs comprehensive exploration within the parameter space, effectively evading local optima and thereby markedly enhancing model generalization. The synergistic interplay between the two algorithms, orchestrated via the "convergence-first, exploration-second" strategy, dynamically balances local exploitation and global exploration. Consequently, the model achieves a comprehensive reduction in prediction error while significantly strengthening its ability to capture the nonlinear dynamics of electrical flux. This dual advancement is ultimately reflected in a substantially improved goodness-of-fit (R^2).

4 Model Validation and Results Discussion

4.1 Experimental Validation

Conch P.O 42.5 ordinary Portland cement with a strength surplus coefficient of 1.10 was used, complying with the GB 175-2020 standard. Its performance indicators are detailed in Table 5. Fine aggregates comprised MS derived from Ningbo tuff and locally sourced natural sand. The MS particle size ranged from 0 to 4.75 mm, conforming to the GB/T 14684-2022 specification. The key properties of the MS are listed in Table 6. CA was composed of continuously graded crushed stone (5–25 mm). The gradation was 20% for the 5–10 mm fraction and 80% for the 10–25 mm fraction. Prior to mixing, aggregates were sieved through a 25 mm screen to remove particles exceeding 25 mm, then rinsed 2–3 times with tap water and dried to remove adherent fines. Class F, Grade I fly ash was sourced from Gongyi Borun Refractory Materials Co., Ltd. Its primary chemical composition was SiO_2, Al_2O_3, SO_3, and CaO. Its physical properties are summarized in Table 7. A polycarboxylate superplasticizer with a water reduction rate of 28% was utilized. Specific test images are shown in Fig. 7.

Table 5: Main properties of the C.

Specific Surface Area m^2/kg	Setting Time/min		Compressive Strength/MPa		Compressive Strength/MPa	
	Initial	Final	3 d	28 d	3 d	28 d
352	260	330	4.8	7.3	21.3	48.1

Table 6: Main performance indicators of the tuff MS.

Fineness Modulus	SPC/%	Apparent Density/(kg/m^3)	Bulk Density/(kg/m^3)	Methylene Blue Value/(g/kg)	Crushing Index/%
2.82	8	2653	1780	2.1	8

Table 7: Key performance indicators of the FA.

Parameter	Density (g/cm^3)	Bulk Density g/cm^3	Fineness (%)	Moisture Content (%)	SiO_2 (%)	Al_2O_3 (%)	CaO (%)	SO_3 (%)
Test Result	2.1	1.10	≤5 μm square-mesh sieve ≤ 18%	≤1	≤50	≥30	≤10	≤3
Specification Requirement	≤2.6	0.63–1.38	16	0.4	45.1	36.8	4.5	1.2

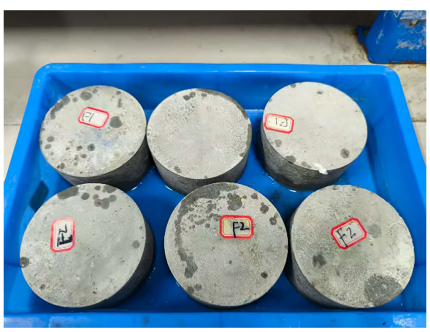

Final Product

Final Product

Figure 7: Test picture.

Prepare 100 mm × 50 mm cylindrical standard concrete specimens and place them in a standard cement concrete curing room with a (20 ± 2)°C and a humidity of ≥95% for curing for 28 days. Subsequently, the electrical flux test was carried out using the DTL-6A concrete electrical flux tester, with 3 specimens in each group. The final result was taken as the average value. The specific mix ratio is as follows (Tables 8–11):

Table 8: MSC mix ratios with different MSR (Group E).

Group	FA kg/m^3	C kg/m^3	W kg/m^3	MS kg/m^3	Natural Sand kg/m^3	CA kg/m^3	Superplasticizer kg/m^3
E0	70	380	150	720	0	1050	9
E10	70	380	150	648	72	1050	9
E20	70	380	150	576	144	1050	9
E30	70	380	150	504	216	1050	9
E40	70	380	150	432	288	1050	9
E50	70	380	150	360	360	1050	9
E60	70	380	150	288	432	1050	9
E70	70	380	150	216	504	1050	9
E80	70	380	150	144	576	1050	9
E90	70	380	150	72	648	1050	9
E100	70	380	150	0	720	1050	9

Table 9: MSC mix ratios of different FA (Group F).

Group	FA kg/m^3	C kg/m^3	W kg/m^3	MS kg/m^3	CA kg/m^3	Superplasticizer kg/m^3
F0	0	450	150	720	1050	9
F10	45	405	150	720	1050	9
F20	90	360	150	720	1050	9
F30	135	315	150	720	1050	9
F40	180	270	150	720	1050	9
F50	225	225	150	720	1050	9

Table 10: MSC mix ratios of different SPC (Group SF).

Group	FA kg/m^3	C kg/m^3	W kg/m^3	MS kg/m^3	SPC %	CA kg/m^3	Superplasticizer kg/m^3
SF0	70	380	150	720	0	1050	9
SF3	70	380	150	698.4	3	1050	9
SF5	70	380	150	684	5	1050	9
SF7	70	380	150	669.6	7	1050	9
SF9	70	380	150	655.2	9	1050	9
SF11	70	380	150	640.8	11	1050	9
SF13	70	380	150	626.4	13	1050	9
SF15	70	380	150	612	15	1050	9
SF17	70	380	150	597.6	17	1050	9

Table 11: MSC mix ratios with different W/C (HF group).

Group	W/C	FA kg/m^3	C kg/m^3	W kg/m^3	MS kg/m^3	CA kg/m^3	Superplasticizer kg/m^3
HF1	0.30	70	430	150	720	1050	9
HF2	0.33	70	380	150	720	1050	8.2
HF3	0.35	70	358	150	720	1050	7.7
HF4	0.38	70	325	150	720	1050	7.1
HF5	0.40	70	305	150	720	1050	6.8

4.2 Experimental Results and Model Validation

The WOA-Adam-BPNN model was employed to predict the EF based on the experimental parameters, and the predictions were compared with the measured values, as presented in Fig. 8. In Group E (MSR as variable), the predicted EF exhibits a "decrease-then-increase" trend with rising MSR, attaining a minimum within the 50%–70% MSR range. For Group F (FA as variable), the EF demonstrates a continuous decreasing trend with higher FA content. In the SF group (SP as variable), the EF similarly shows a "decrease-then-increase" pattern with increasing SP, reaching a minimum between 7% and 11% SPC. For the HF group (W/C as variable), as W/C increases from 0.3 to 0.4, the EF again follows a "decrease-then-increase" trend, with a clear minimum at a W/C of 0.33.

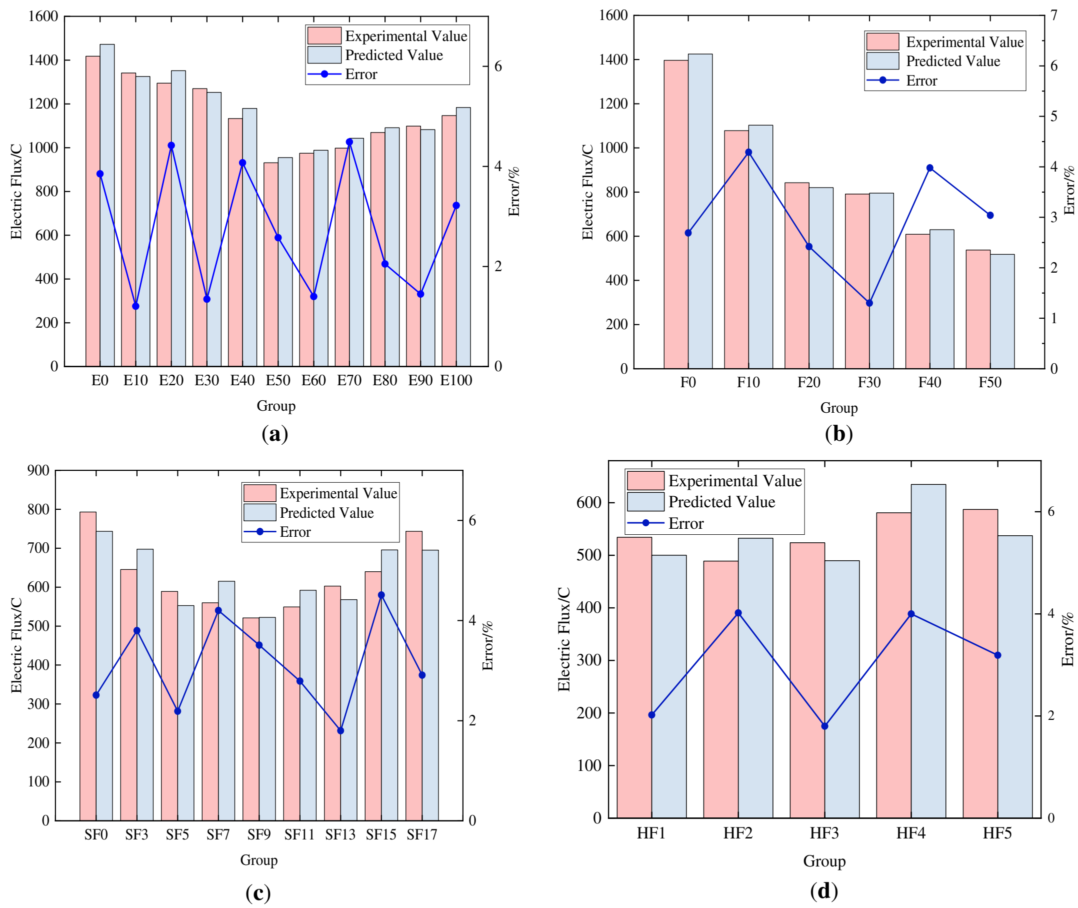

Figure 8: Comparison between predicted and actual EF values. (**a**) Group E; (**b**) Group F; (**c**) Group SF; (**d**) Group HF.

Analysis across all specimen groups (E, F, SF, HF) indicates that the WOA-Adam-BPNN model delivers outstanding predictive performance and robust generalization across varying MSR levels and mix proportions. A strong agreement between predicted and experimental values is observed for all groups. Quantitatively, the maximum and minimum prediction errors for each group are as follows: Group E, 4.49% and 1.20%; Group F, 3.98% and 1.30%; Group SF, 4.51% and 2.19%; Group HF, 4.02% and 2.02%. These results collectively confirm the model's efficacy for reliable EF prediction in MSC. Moreover, the predicted variation trends of EF with key parameters are highly consistent with the physical mechanisms of chloride ion penetration in MSC, which verifies the rationality of the model results from the perspective of material physics.

4.3 Interpretability Analysis

This study employed SHAP value analysis to quantify the influence of material parameters on the chloride ion penetration resistance of MSC, with EF as the prediction target. The results are summarized in Fig. 9.

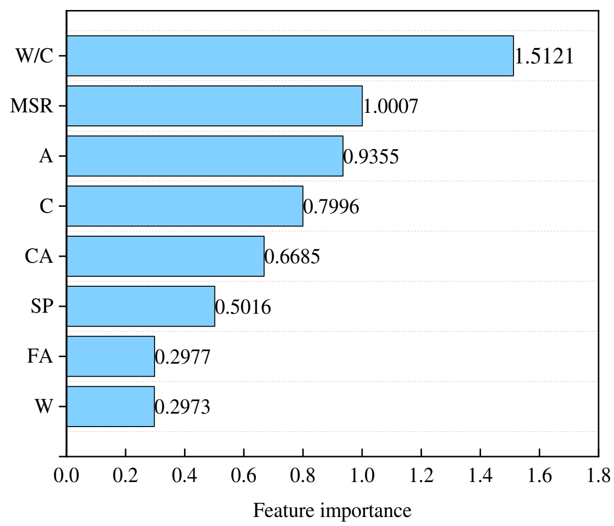

Figure 9: SHAP value for each input feature.

With a SHAP value of 1.5125, W/C emerges as the most dominant factor. It significantly impedes chloride ion migration by directly governing the pore structure and density of the cement paste. MSR (SHAP = 1.0007) ranks second, primarily affecting the characteristics of the interfacial transition zone and the overall packing density. The dosages of A (0.9355) and C (0.7996) jointly modulate the paste rheology and hydration process, thereby collaboratively optimizing the microstructure. In contrast, CS dosage (0.6685) and SPC (0.5016) exert a moderate influence through skeleton and filler effects. The influence of FA (0.2977) and W (0.2951) is relatively weaker within the context of this model. This attenuated influence may be due to the overshadowing of water's role by the dominant W/C and the long-term, progressive nature of FA's pozzolanic reaction.

Therefore, to enhance the chloride ion penetration resistance of MSC, priority should be given to the stringent control of W/C and the optimization of MSR. A systematic durability improvement can then be achieved through a multi-scale collaborative design of the mix proportion.

Beyond the quantitative importance ranking from SHAP values, the physical mechanisms governing chloride penetration in MSC are interpreted by linking key parameters to chloride transport, pore structure evolution, and interfacial transition zone (ITZ) characteristics, bridging data-driven results with fundamental diffusion physics.

As the dominant factor, W/C controls hydration and pore formation. A higher W/C causes incomplete hydration, increases connected macropores, reduces diffusion path tortuosity, and accelerates penetration per Fick's second law. In MSC, an appropriate W/C promotes the pozzolanic reaction between stone powder and $Ca(OH)_2$ to form more C-S-H gel, densifying the matrix and decreasing the effective chloride diffusion coefficient.

MSR affects transport via ITZ and packing density. Proper MSR optimizes gradation and reduces ITZ porosity, while excessive MSR leads to stone powder agglomeration and porous ITZ, forming fast chloride pathways. SPC provides micro-filling and hydration effects. Moderate SPC refines pores, whereas excessive SPC increases water demand and capillary porosity, weakening impermeability. Other parameters influence penetration indirectly by altering paste compactness and ITZ stability. FA shows limited influence because its long-term pore-refining effect is not fully developed at the test age.

Notably, the dominance of W/C is not a trivial repetition of existing knowledge. In MSC, the strong coupling between W/C, stone powder content, and MSR makes W/C particularly critical for pore structure and ITZ densification, distinguishing this work from conventional natural sand concrete.

5 Conclusions

This study constructs a WOA-Adam-BPNN model to predict the chloride ion penetration resistance of manufactured sand concrete (MSC), revealing the influence patterns of key parameters such as water-cement ratio and manufactured sand replacement rate.

1. This study proposes a WOA-Adam dual-stage collaborative hybrid optimization model for predicting the chloride ion penetration resistance of manufactured sand concrete (MSC). The model synergistically integrates the global exploration capability of the whale optimization algorithm with the rapid local convergence of the Adam optimizer, effectively mitigating the tendency of traditional back-propagation neural networks to converge to local optima.
2. The proposed model demonstrates excellent predictive performance and generalization capability. It achieves a MAPE of 4.01%, MAE of 45.09, RMSE of 59.57, and an R^2 of 0.9879. Compared to Adam-BPNN, GA-Adam-BPNN, and WOA-XGB, the MAPE reductions are 77.3%, 61.0%, and 52.5%, respectively, with corresponding R^2 improvements of 15.4%, 9.4%, and 6.2%. Experimental validation across four groups of mix proportions shows that the prediction error remains consistently below 5% within the investigated parameter ranges (MSR: 0%–100%, FA: 0%–50%, SPC: 0%–17%, W/C: 0.30–0.40).
3. Experimental analysis reveals the influence patterns of key parameters on chloride ion penetration. Water-cement ratio emerges as the dominant factor, followed by manufactured sand replacement rate and stone powder content, with their coupling effects critically influencing pore structure and interfacial transition zone characteristics. However, due to limitations in available literature, finer quality characteristics of manufactured sand (e.g., particle shape, gradation, MB value) are not fully incorporated. Future work will expand the dataset to include these indicators and employ k-fold cross-validation to further enhance model applicability.

Acknowledgement: The authors would like to thank all individuals and organizations that contributed to this study through administrative and technical assistance, as well as material or equipment support. Their contributions were essential to the successful completion of this research.

Funding Statement: The work was supported by the Natural Science Foundation of Ningbo (Grant No. 2023J041) and the Ningbo Construction Research Project (Grant Nos. 2024-20, 2024-23).

Author Contributions: Zhichao Liu: Writing—original draft, Visualization, Validation. Jun Zhang: Methodology, Formal analysis, Data curation, Conceptualization. Dongling Yu, Libing Jin and Bingquan Song: Supervision, Software, Resources. All authors reviewed and approved the final version of the manuscript.

Availability of Data and Materials: Data available on request from the authors.

Ethics Approval: This study involves the collection of durability data for manufactured sand concrete, the establishment of a hybrid optimization model, and its engineering applicability validation. It does not involve human or animal experiments, nor the use of any sensitive materials. Therefore, formal ethical approval was not required. All experiments were conducted in accordance with standard engineering practices and safety regulations.

Conflicts of Interest: The authors declare no conflicts of interest.

References

1. Gu XL, Zhou T, Nagai K, Zhang H, Yu QQ. Prediction of seismic performance of a masonry-infilled RC frame based on DEM and ANNs. Eng Struct. 2024;316(3):118531. doi:10.1016/j.engstruct.2024.118531.
2. Shi F, Wang Y, Pei L, Geng F, Xue Y. A support vector regression-based method for stone powder detection in machine-made sand. In: Intelligent transportation and smart cities. Amsterdam, The Netherlands: IOS Press; 2024. doi:10.3233/atde240395.
3. Kuang W, Pavlenko P, Guo H, Tian K, Liu H, Zhou Z, et al. Utilization of machine-made sand waste in 3D-printed ecological concrete for artificial reefs. Case Stud Constr Mater. 2025;22(37):e04494. doi:10.1016/j.cscm.2025.e04494.
4. Song SM, Hu YY. Progress in standardized technology for manufactured sand and reflections on related issues. J Build Mater. 2025;28(7):628–34. (In Chinese). doi:10.1360/n972015-00105.
5. Gong L, Li Z, Ran B, Xu T, Bu Y, Zhao X. Research on frost resistance of desert sand and sandy sand concrete and lifetime prediction. Results Eng. 2025;28(6):107136. doi:10.1016/j.rineng.2025.107136.
6. Liang J, Lin J, Lv J, Zheng S, Rong H, Yang X. Research on rebound strength measurement curve of modified carbonation depth of machine-made sand concrete. J Mater Civ Eng. 2024;36(5):05024004. doi:10.1061/jmcee7.mteng-16919.
7. Yuan Z, Zheng W, Qiao H. Machine learning based optimization for mix design of manufactured sand concrete. Constr Build Mater. 2025;467(5):140256. doi:10.1016/j.conbuildmat.2025.140256.
8. Ren Q, Ding L, Dai X, Li C, Li C, Jiang Z. Optimizing mix design of concrete with manufactured sand for low embodied carbon and desired strength using machine learning. Constr Build Mater. 2024;457:139407. doi:10.1016/j.conbuildmat.2024.139407.
9. Liu C, Liu P, Tang K, Guan S, Luo X, Zhang L, et al. Carbonation curing and long-term shrinkage performance of manufactured sand concrete with different strength grades from tunnel muck. Constr Build Mater. 2025;467:140406. doi:10.1016/j.conbuildmat.2025.140406.
10. Zhang W, Wu C, Li Y, Wang L, Samui P. Assessment of pile drivability using random forest regression and multivariate adaptive regression splines. Georisk Assess Manag Risk Eng Syst Geohazards. 2021;15(1):27–40. doi:10.1080/17499518.2019.1674340.
11. Hong WK, Nguyen MC, Pham TD. Pre-tensioned concrete beams optimized with a unified function of objective (UFO) using ANN-based Hong-Lagrange method. J Asian Archit Build Eng. 2024;23(5):1573–95. doi:10.1080/13467581.2023.2270028.
12. Hao M, Li Y, Chen X, Ni K, Li W. Optimization design method of C30/C40 fly ash concrete based on machine learning and elite retention genetic algorithm. Adv Eng Softw. 2025;210:104019. doi:10.1016/j.advengsoft.2025.104019.

13. Al-Taai SR, Azize NM, Thoeny ZA, Imran H, Bernardo LFA, Al-Khafaji Z. XGBoost prediction model optimized with Bayesian for the compressive strength of eco-friendly concrete containing ground granulated blast furnace slag and recycled coarse aggregate. Appl Sci. 2023;13(15):8889. doi:10.3390/app13158889.
14. Lyngdoh GA, Zaki M, Anoop Krishnan NM, Das S. Prediction of concrete strengths enabled by missing data imputation and interpretable machine learning. Cem Concr Compos. 2022;128:104414. doi:10.1016/j.cemconcomp.2022.104414.
15. Tian H, Qiao H, Zhang Y, Feng Q, Wang P, Xie X. Predicting the impermeability and mechanical properties of manufactured sand polymer waterproof mortar using an optimised back-propagation neural network. Constr Build Mater. 2024;441(1):137475. doi:10.1016/j.conbuildmat.2024.137475.
16. Jiang S, Zhang J, Cui Z, Yu D, Jin L, Song B. Compressive strength prediction of machine-made sand concrete based on a Bayesian Optimization-Stacking model. Case Stud Constr Mater. 2025;23:e05516. doi:10.1016/j.cscm.2025.e05516.
17. Wang S, Ge Y, Srinivasakannan C, Guo J, Han M, Yuan J, et al. Modeling and simulation of a multi source microwave heating of soil based on PSO-BPNN. Appl Therm Eng. 2024;257:124148. doi:10.1016/j.applthermaleng.2024.124148.
18. Zheng W, Cai J. A optimum prediction model of chloride ion diffusion coefficient of machine-made sand concrete based on different machine learning methods. Constr Build Mater. 2024;411(1):134414. doi:10.1016/j.conbuildmat.2023.134414.
19. Li K, Ye W. Improving efficiency in structural optimization using RBFNN and MMA-Adam hybrid method. Adv Eng Inform. 2024;62(3):102869. doi:10.1016/j.aei.2024.102869.
20. Akshya J, Neelamegam G, Sureshkumar C, Nithya V, Kadry S. Enhancing UAV path planning efficiency through Adam-optimized deep neural networks for area coverage missions. Procedia Comput Sci. 2024;235(1):2–11. doi:10.1016/j.procs.2024.04.001.
21. Wang X, Wang Y, Yu H, Li C, Gao X, Li L. Quantitative assessment on performance and cracking potential of tuff manufactured sand concrete. J Harbin Inst Technol. 2023;55(11):25. (In Chinese). doi:10.11918/202112041.
22. Liu QS, Lu FL, Liu ZJ. Influence of stone powder content on the durability of machine-made sand self compacting concrete. Concrete. 2023;(5):92–5. (In Chinese).
23. Li B, Wang J, Zhou M. Effect of limestone fines content in manufactured sand on durability of low- and high-strength concretes. Constr Build Mater. 2009;23(8):2846–50. doi:10.1016/j.conbuildmat.2009.02.033.
24. Liu Z. Effect of machine-made sand rate on the compressive strength, workability, and impermeability of sleeper concrete. In: Frontier research on high performance concrete and mechanical properties. Singapore: Springer Nature; 2024. p. 141–9. doi:10.1007/978-981-97-4090-1_13.
25. Zhang M, Gao S, Liu T, Guo S, Zhang S. High-performance materials improve the early shrinkage, early cracking, strength, impermeability, and microstructure of manufactured sand concrete. Materials. 2024;17(10):2465. doi:10.3390/ma17102465.
26. Li WY, Cheng LK, Liu HH, Mu JW, Zhang KY, Ren Q, et al. Effect of limestone powder as mineral admixture on mechanical properties and durability of concrete with manufactured sand. Concrete. 2024;(7):82–6. (In Chinese).
27. Ge W, Zhu S, Yang J, Ashour A, Zhang Z, Li W, et al. Mechanical properties and durability of sustainable UHPC using industrial waste residues and sea/manufactured sand. J Test Eval. 2024;52(2):1064–94. doi:10.1520/jte20230450.
28. Walters GH, Jones TR. Effect of metakaolin on alkali-silica reaction (ASR) in concrete manufactured with reactive aggregate. Int Concr Abstr Portal. 1991;126:941–54. doi:10.14359/2454.
29. Narale PU, Jadhav HS. Durability studies concerning permeability on high performance concrete using artificial sand as fine aggregate. In: Sustainability trends and challenges in civil engineering. Singapore: Springer; 2021. p. 325–37. doi:10.1007/978-981-16-2826-9_21.
30. Li H, Wang Z, Huang F, Yi Z, Xie Y, Sun D, et al. Impact of different lithological manufactured sands on high-speed railway box girder concrete. Constr Build Mater. 2020;230(6):116943. doi:10.1016/j.conbuildmat.2019.116943.
31. Li H, Huang F, Cheng G, Xie Y, Tan Y, Li L, et al. Effect of granite dust on mechanical and some durability properties of manufactured sand concrete. Constr Build Mater. 2016;109(6):41–6. doi:10.1016/j.conbuildmat.2016.01.034.

32. Chang X, He T, Niu M, Zhao L, Wang L, Wang Y. Influence of limestone powder mixing method on properties of manufactured sand concrete. Case Stud Constr Mater. 2024;20(4):e02996. doi:10.1016/j.cscm.2024.e02996.
33. Zhu Y, Wang P, Guo H, Lou R, Ye W, Liu Y, et al. Effect of dry process manufactured sands dust on the mechanical property and durability of recycled concrete. J Build Eng. 2024;87(1):108942. doi:10.1016/j.jobe.2024.108942.
34. Shen W, Wu J, Du X, Li Z, Wu D, Sun J, et al. Cleaner production of high-quality manufactured sand and ecological utilization of recycled stone powder in concrete. J Clean Prod. 2022;375:134146. doi:10.1016/j.jclepro.2022.134146.
35. Dinh HL, Liu J, Ong DEL, Doh JH. A sustainable solution to excessive river sand mining by utilizing by-products in concrete manufacturing: a state-of-the-art review. Clean Mater. 2022;6:100140. doi:10.1016/j.clema.2022.100140.
36. Raja R, Vijayan P, Kumar S. Durability studies on fly-ash based laterized concrete: a cleaner production perspective to supplement laterite scraps and manufactured sand as fine aggregates. J Clean Prod. 2022;366(4):132908. doi:10.1016/j.jclepro.2022.132908.
37. Sun Y, Song S, Yu H, Ma H, Xu Y, Zu G, et al. Experimental study on the strength and durability of manufactured sand HPC in the Dalian Bay undersea immersed tube tunnel and its engineering application. Materials. 2024;17(20):5003. doi:10.3390/ma17205003.
38. Zheng S, Chen J, Wang W. Effects of fines content on durability of high-strength manufactured sand concrete. Materials. 2023;16(2):522. doi:10.3390/ma16020522.
39. Wu QY, Zhao S, Wang W, Qiao M, Chen JS, Du S. Preparation and durability study of C30 tunnel slag mechanized sand sprayed concrete. Concrete. 2025;(8):164–9. (In Chinese).
40. Wang Z, Li HJ, Huang FL, Yi ZL, Yang ZQ. Study on properties of concretes with manufactured sands with typical lithology in railway engineering. J China Railw Soc. 2024;46(7):159–66. (In Chinese).
41. Yang ZF, Li SK, Zhao H. Effect of mica content in machine-made sand on mechanical and durability properties of C50 concrete. Highway. 2025;70(8):350–4. (In Chinese).
42. Yan YD, Wang X, Lu CH, Tao ST, Ji GQ. Resistance of manufactured sand concrete with fly ash to chloride ion attack under dry-wet cycle. J Jiangsu Univ Nat Sci Ed. 2023;44(6):731–7. (In Chinese).
43. Yu Z, Sun JT, Wu DL, Lu ZL, He T, Li ZT, et al. Effect of clay powder in manufactured sand on properties of mortar and concrete. Bull Chin Ceram Soc. 2023;42(7):2372–81. (In Chinese). doi:10.3390/ma15134593.
44. Zhao L, Sun JT, Wu DL, Li ZT, He T, Guan YC, et al. Preparation and performance of stone chips wet shotcrete. Bull Chin Ceram Soc. 2023;42(3):1016–24. (In Chinese).
45. Huang WR, He YX, Cui JD, Chen H, Yan MH, Wang J. Study on long-term performance of C50 machine-made sand self-compacting concrete. Concrete. 2022;(11):106–9 114. (In Chinese).
46. Luo J, Yu B, Su J, Liu T, Xie C, Zhang K. Influence of machine-made sand particle size distribution on concrete performance. Highway. 2022;67(12):384–8. (In Chinese). doi:10.1051/e3sconf/202123301040.
47. Wang LC, Fu L, Wang YL, Zhang XM, Deng BL. Experimental study on durability of machine-made sand concrete for railway tunnel lining. Chin J Undergr Space Eng. 2021;17(6):1857–63. (In Chinese).
48. Yu BT, Liu T, Wang H, Xie C, Li S. Influence of granite porphyry stone powder content on properties and microstructure of concrete. J Jilin Univ Eng Technol Ed. 2022;52(5):1052–62. (In Chinese).
49. Tong XG, Zhang KF, Meng G, Luo ZQ, Hu YB, Wang JM, et al. Influence of manufactured sand-stone chips composite fine aggregate on properties of different strength grade concrete. Bull Chin Ceram Soc. 2021;40(4):1205–12+1227. (In Chinese).
50. Guo RP, Zhang YZ, Xia JL, Zhou YX. Study on the influence of machine-made sand powder content on the performance of sleeper concrete. Concrete. 2020;2020(8):113–6. (In Chinese).
51. Zhang PJ, Zhang XJ, Song SL, Luan JH, Nan XL, Han B. Effect of green mudstone powder content in manufactured sand on mechanical properties and durability of concrete. Bull Chin Ceram Soc. 2020;39(1):61–7. (In Chinese).
52. Wang CQ, Gao HL. Experimental study on preparation of super high pumping concrete with machine-made sand. Concrete. 2019;2019(6):112–4. (In Chinese).
53. Xu X, Xia JL, Zhou YX, Leng FG, Wu ZX. Study on the preparation and properties of C55 concrete of mechanism sand T beam. Concrete. 2019;2019(4):134–7. (In Chinese).

54. Li JH, Zhang BS, Wang YD, Gao C, Zhou YX, He Y, et al. Study on mixture ratio design and performance of manufactured sand concrete with high content of limestones. Bull Chin Ceram Soc. 2018;37(11):3641–5+3651. (In Chinese). doi:10.4028/www.scientific.net/kem.405-406.204.
55. Yan JJ, Deng C, Ye XS. Study on effects of specific surface area of stone dust on the properties of cement mortar. China Concr Cem Prod. 2018;2018(3):7–10. (In Chinese).
56. Yang L, Tan YB, Qiu ZX, Li HJ, Wang Z, Xie YJ. Study on performance of concrete with high stone powder content using manufactured sand. Railw Eng. 2015;55(8):119–22. (In Chinese).
57. Zhou H, Ge C, Chen Y, Song X. Study on performance and fractal characteristics of high-strength manufactured sand concrete with different MB values. Front Earth Sci. 2023;11:1140038. doi:10.3389/feart.2023.1140038.
58. Feng J, Dong C, Chen C, Wang X, Qian Z. Effect of manufactured sand with different quality on chloride penetration resistance of high-strength recycled concrete. Materials. 2021;14(22):7101. doi:10.3390/ma14227101.
59. Chandrasekhar C, Ransinchung GD. Assessment of interface characteristics and durability aspects of manufactured sand (M-sand) in engineered cementitious composites. J Build Eng. 2024;91:109705. doi:10.1016/j.jobe.2024.109705.
60. Liu T, Zhu L, Yu B, Li T. Experimental studies to investigate efficacies of granite porphyry powder as homologous manufactured sand substitute. J Adv Concr Technol. 2023;21(4):307–21. doi:10.3151/jact.21.307.
61. Shanmugapriya T, Raja KS, Balaji C. Strength and durability properties of high performance concrete with manufactured sand. ARPN J Eng Appl Sci. 2016;11(9):6036–45. doi:10.1007/978-981-19-6313-1_4.
62. Shanmugavadivu PM, Malathy R. Effects of chloride attack on concrete with the replacement of natural sand by manufactured sand as fine aggregate. J Struct Eng. 2012;39(5):564–73.
63. Zhang M, Xu J, Li M, Yuan X. Influence of stone powder content from manufactured sand concrete on shrinkage, cracking, compressive strength, and penetration. Buildings. 2023;13(7):1833. doi:10.3390/buildings13071833.
64. Xu GQ, Qiao L, Liu JH, Wang XL. Experiment on C40 machine-made sand concrete with combined admixture of limestone powder and substandard fly ash. Adv Mater Res. 2010;152–153:996–9. doi:10.4028/www.scientific.net/amr.152-153.996.
65. Balasubramaniam T, Thirugnanam GS. Durability studies on bottom ash concrete with manufactured sand as fine aggregate. J Ind Pollut Control. 2015;31(1):69–72.
66. Qu F, Yang Y, Song W, Liu J, Ma L, Ding X. Experimental study on application of machine-made sand concrete in PCCP. J North China Univ Water Resour Electr Power. 2022;43(6):19–23. (In Chinese). doi:10.19760/j.ncwu.zk.2022058.
67. Jiang TH, Yang XF, Yang JD, Qian FH, Ping Y, Yang TY, et al. Effects of stone powder type and content on C60 manufactured sand concrete performance. Bull Chin Ceram Soc. 2023;42(1):92–9. (In Chinese).